Exploration of the relationship between inertia enhancement and DC-link capacitance for grid-connected converters

Guo, Ke; Tang, Yi; Fang, Jingyang

2018

Guo, K., Tang, Y., & Fang, J. (2018). Exploration of the relationship between inertia enhancement and DC-link capacitance for grid-connected converters. 2018 IEEE 4th Southern Power Electronics Conference (SPEC). doi:10.1109/SPEC.2018.8635904

https://hdl.handle.net/10356/82614

https://doi.org/10.1109/SPEC.2018.8635904

Exploration of the Relationship Between Inertia Enhancement and DC-Link Capacitance for Grid-Connected Converters

Ke Guo
Energy Research Institute @ NTU, ERI@N
Interdisciplinary Graduate School
Nanyang Technological University
Singapore
ke004@e.ntu.edu.sg

Yi Tang and Jingyang Fang
School of Electrical and Electronic Engineering
Nanyang Technological University
Singapore
yitang@ntu.edu.sg, jfang006@e.ntu.edu.sg

***Abstract*— Grid-connected converters (GCCs) are showing potential in providing virtual inertia and has attracted wide attention recently. For the virtual inertia emulated by GCCs, it is proportional with the DC-link capacitance, and thus, the DC-link capacitance can directly affect the dynamic performance for the GCC emulating inertia through modifying the inertia constant. However, the impacts of the DC-link capacitance have never been discussed in any literature before. Considering this issue, the influence of the DC-link capacitance on the dynamic performance for the GCC providing virtual inertia is analyzed in this paper. In addition to that, the selection approach of the DC-link capacitance is presented by tuning the system damping ratio within its optimal range. Simulations verify the correctness.**

Keywords—grid-connected converters (GCCs); virtual inertia; DC-link capacitance; dynamic performance

I. INTRODUCTION

Along with the huge consumption of fossil energy resources in the modern society, carbon emission has grown into one of the major global concerns [1]. To settle this issue, growing amount of renewable energy sources (RESs) is integrating into power grids, and the modern power system is transforming from the synchronous generation dominated structure to the mixed structure consisting of synchronous and non-synchronous generation [2]. In the conventional power system dominated by the synchronous generation, the kinetic energy stored in the rotating masses of synchronous generators (SGs) can provide inertia support in emergency, and hence the stability of power systems can be maintained after faults [3]. However, due to the variable and uncertain availability of RESs, renewable generators such as wind turbines (WTs) and photovoltaic (PV) panels are decoupled from power grids by power converters, consequently, no inertia can be contributed to power systems naturally [4]. With large number of SGs replaced by such renewable generators, the total inertia of power grids declines remarkably, and the ever-decreasing inertia will further lead to low frequency nadir and excessive rate of change of frequency (RoCoF), which may cause generator tripping and even the grid collapse [5].

As increasing inertia is very desirable, the concept of virtual inertia has been proposed by Beck and Hesse in 2007 [6], and various control architectures have been developed since then. In [7, 8], the pitch angles of WTs are tightly controlled, so that part of the wind power is reserved for inertia emulation. In [9, 10], a deloading factor is imposed on the maximum power point tracking (MPPT) algorithm of renewable generators, and the trimmed part of the output power is retained for inertial power supply in emergency. However, the deloading scheme requires curtailment of the output power from renewable generators and results in additional opportunity costs. Another approach to emulate inertia is exploiting the kinetic energy stored in the rotors of WTs. It is shown in [11] that the kinetic energy stored in the spinning rotors of WTs is far more than that of conventional SGs, and this kind of kinetic energy can be utilized to provide inertia response. A controller is designed for doubly fed induction generators (DFIGs) in [12] to regulate the rotor speed of WTs in proportion to the grid frequency deviation and the RoCoF, so that the kinetic energy can be released for frequency regulation. In [13], the rotor speed control loop for permanent magnet synchronous generators (PMSGs) is presented to mimic inertia. Although these approaches make good use of the kinetic energy of WTs for inertia emulation, the changes of rotor speed increase the wear and tear and reduce the lifetime of WTs [14].

Recently, the virtual inertia emulated by grid-connected converters (GCCs) is also showing great potential and attracts a lot of attention. The concept of the distributed virtual inertia control realized by GCCs is detailed with its effectiveness verified in [15]. This method features no change of hardware, and hence it is economically attractive. Along with this approach, the electromagnetic energy stored in the DC-link capacitor is utilized for inertia response, and the value of the emulated inertia is proportional with the capacitance of the DC-link capacitor. According to [16], the dynamic frequency response during disturbance has great relations with the inertia constant, therefore, for GCCs providing virtual inertia, the capacitance of the DC-link capacitors can affect the dynamics performance remarkably through modifying the emulated inertia. However, to the best knowledge of authors, such

978-1-5386-8257-9/18/$31.00 ©2018 IEEE

influence of the DC-link capacitance on the GCCs providing virtual inertia has never been discussed in any literature previously.

In light of this issue, the impacts of the DC-link capacitance on the dynamic performance for the GCCs providing virtual inertia are analyzed in this paper. The small signal model of the power system including virtual inertia generated from GCCs is derived, and the relationships between critical dynamic indices regarding the DC-link capacitance are investigated in detail. In addition to that, the selection approach of the DC-link capacitance through tuning the damping ratio to be within its optimal range is also presented. Finally, simulation results verify the correctness.

II. System Model and Virtual Inertia Provided by GCCs

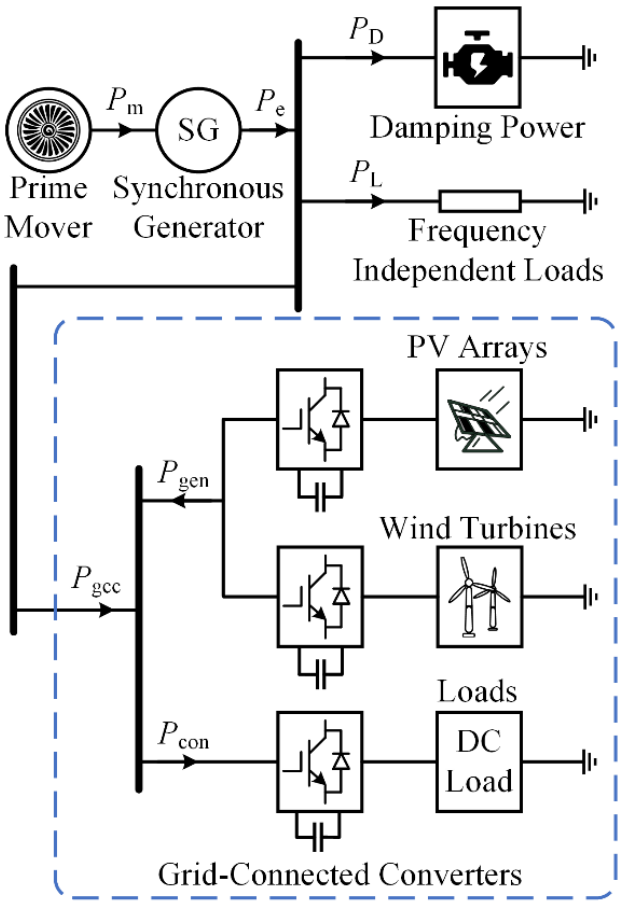

Fig. 1. The schematic of a typical power system.

The simplified schematic of a typical power system consisting of the synchronous generation and GCC-coupled components is depicted in Fig. 1, in which P_M denotes the input mechanical power of the SG, P_D represents the power absorbed by the frequency-dependent loads, P_L is the power consumed by the frequency-independent loads. P_{GCC} denotes the power consumed by the GCC coupled components. For the synchronous generation part shown in Fig. 1, the dynamics are characterized by the swing equation (in per unit and the same below):

$$\Delta P_M - \Delta P_D - \Delta P_L = 2H\frac{d\Delta f}{dt} \tag{1}$$

where Δ signifies the variation. Δf refers to the frequency deviation. H stands for the inertia constant.

It has been proven in [15] that the virtual inertia generated by GCCs has great potential in power system inertia enforcement. For illustration, the block diagram of the GCC equipped with the virtual inertia control is shown in Fig. 2.

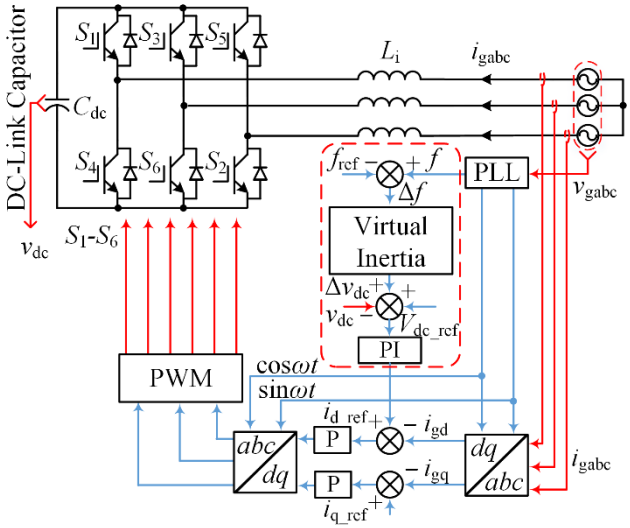

Fig. 2. Block diagram of the GCC equipped with the virtual inertia control.

In Fig. 2, the three-phase voltages are measured by a phase-locked loop (PLL), providing the phase angle information for grid synchronization and coordinate transformation. The GCC is controlled in dq-frame with a cascaded control architecture [4], and the DC-link voltage v_{dc} can be regulated by modifying the d-axis reference current i_{d_ref}. In order to enable the GCC to respond to power system disturbances, a virtual inertia control block is reported in [15] to exploit the energy stored in the DC-link capacitor for inertia emulation, and the inertial power supplied by the DC-link capacitor of the GCC is expressed as:

$$\Delta P_{GCC} = \frac{C_{dc}V_{dc\_ref}^{\ 2}}{VA_{rated}}\frac{dv_{dc}}{dt} = 2H_c\frac{dv_{dc}}{dt} \tag{2}$$

where C_{dc}, v_{dc}, and V_{dc_ref} are the DC-link capacitance, DC-link voltage, and nominal voltage of the DC-link capacitor, respectively. VA_{rated} stands for the rated power of the GCC. H_c denotes the inertia constant of the DC-link capacitor, and it can be expressed as:

$$H_c = \frac{C_{dc}V_{dc\_ref}^{\ 2}}{2VA_{rated}} \tag{3}$$

A proportional controller is employed in the virtual inertia control block to relate the DC-link voltage directly with the grid frequency deviation, defined as:

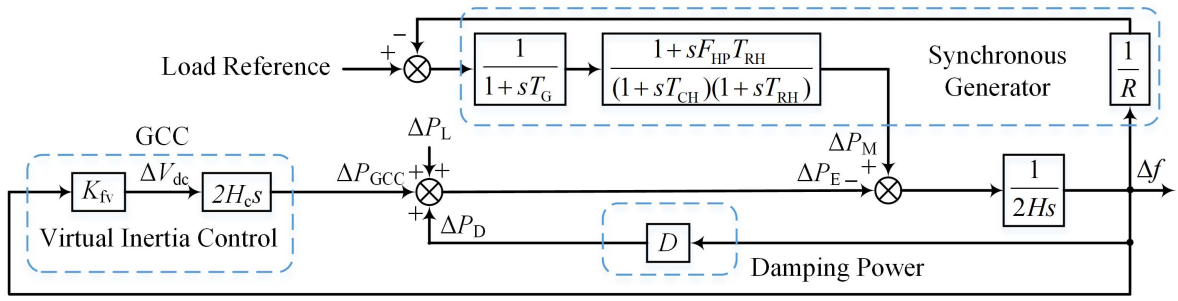

Fig. 3. Block diagram of the frequency regulation with the virtual inertia from GCCs.

$$K_{\mathrm{fv}}=\frac{\Delta V_{\mathrm{dc\_max}}}{\Delta f_{\mathrm{max}}} \tag{4}$$

where $\Delta V_{\mathrm{dc\_max}}$ and Δf_{max} are the maximum DC-link voltage deviation and maximum grid frequency variation, respectively.

Therefore, the virtual inertia constant emulated by the GCC can be derived as:

$$H_{\mathrm{vi}}=K_{\mathrm{fv}}H_{\mathrm{c}}=\frac{\Delta V_{\mathrm{dc\_max}}}{\Delta f_{\mathrm{max}}}\cdot\frac{C_{\mathrm{dc}}V_{\mathrm{dc\_ref}}^{\ 2}}{2VA_{\mathrm{rated}}} \tag{5}$$

Furthermore, by taking the additional inertial power ΔP_{GCC} generated from the GCC into consideration, the swing equation represented by (1) is modified as:

$$\begin{aligned}&\Delta P_{\mathrm{M}}-\Delta P_{\mathrm{D}}-\Delta P_{\mathrm{L}}-\Delta P_{\mathrm{GCC}}=2H\frac{d\Delta f}{dt}\\&\Rightarrow\Delta P_{\mathrm{M}}-\Delta P_{\mathrm{D}}-\Delta P_{\mathrm{L}}=2(H+H_{\mathrm{vi}})\frac{d\Delta f}{dt}\end{aligned} \tag{6}$$

From (6), with the extra power contributed by the GCC, the inertia constant of the power system increases from H to $(H+H_{\mathrm{vi}})$. The block diagram of frequency regulation with the virtual inertia from GCCs is illustrated in Fig. 3, in which R, T_{G}, T_{CH}, T_{RH} and F_{HP} are coefficients of the reheat turbine based SG [3]; D is the damping factor.

III. Impacts of the DC-Link Capacitance on the Dynamic Performance

A. Impacts of the DC-Link Capacitance

According to (3) and (5), it can be observed that the virtual inertia constant H_{vi} emulated by the GCC is proportional with the DC-link capacitance C_{dc} once other parameters such as $\Delta V_{\mathrm{dc\_max}}$, Δf_{max}, $V_{\mathrm{dc\_ref}}$ and VA_{rated} are fixed. Therefore, the dynamic performance of the GCC providing virtual inertia is in great relationship with the DC-link capacitance C_{dc}.

Based on the Fig. 3, the transfer function $G_{\mathrm{PL\to f}}(s)$ from power deviation ΔP_{L} to frequency deviation Δf is derived as:

$$G_{\mathrm{PL\to f}}(s)=\frac{\Delta f}{\Delta P_{\mathrm{L}}}=\frac{-R(1+T_{\mathrm{G}}s)(1+T_{\mathrm{CH}}s)(1+T_{\mathrm{RH}}s)}{\left[\begin{array}{l}R(1+T_{\mathrm{G}}s)(1+T_{\mathrm{CH}}s)(1+T_{\mathrm{RH}}s)\cdot\\(2Hs+2H_{\mathrm{c}}K_{\mathrm{fv}}s+D)+F_{\mathrm{HP}}T_{\mathrm{RH}}s+1\end{array}\right]} \tag{7}$$

According to [17], the poles associated with T_{G} and T_{CH} has little influence in the analysis of frequency response and can be neglected. Therefore, $G_{\mathrm{PL\to f}}(s)$ expressed in (7) can be simplified to second order, expressed as:

$$\begin{aligned}G_{\mathrm{PL\to f}}(s)&=\frac{-R(1+T_{\mathrm{RH}}s)}{R(1+T_{\mathrm{RH}}s)(2Hs+2H_{\mathrm{c}}K_{\mathrm{fv}}s+D)+F_{\mathrm{HP}}T_{\mathrm{RH}}s+1}\\&=G_0\frac{s+z_1}{s^2+2\xi\omega_{\mathrm{n}}s+\omega_{\mathrm{n}}^{\ 2}}\end{aligned} \tag{8}$$

where G_0 is the DC gain, ω_{n} denotes the natural frequency, and ξ stands for the damping ratio, expressed as the following:

$$\begin{cases}G_0=-\dfrac{1}{2H+2H_{\mathrm{c}}K_{\mathrm{fv}}}\\\omega_{\mathrm{n}}=\sqrt{\dfrac{DR+1}{RT_{\mathrm{RH}}(2H+2H_{\mathrm{c}}K_{\mathrm{fv}})}}\\\xi=\dfrac{RT_{\mathrm{RH}}D+R(2H+2H_{\mathrm{c}}K_{\mathrm{fv}})+F_{HP}T_{\mathrm{RH}}}{2RT_{\mathrm{RH}}(2H+2H_{\mathrm{c}}K_{\mathrm{fv}})\omega_{\mathrm{n}}}\end{cases} \tag{9}$$

Considering a step-up load change, the grid frequency can be expressed in the s domain as:

$$\begin{aligned}f(s)&=f_{\mathrm{ref}}(s)+\Delta f(s)=\frac{1}{s}+G_{\mathrm{PL\to f}}(s)\cdot\frac{1}{s}\\&=\frac{1}{s}+G_0\left\{\begin{array}{l}\dfrac{1}{\omega_{\mathrm{d}}}\cdot\dfrac{\omega_{\mathrm{d}}}{(s+\zeta\omega_{\mathrm{n}})^2+\omega_{\mathrm{d}}^{\ 2}}+\dfrac{z_1}{\omega_{\mathrm{n}}^{\ 2}}\cdot[\dfrac{1}{s}-\\\dfrac{s+\zeta\omega_{\mathrm{n}}}{(s+\zeta\omega_{\mathrm{n}})^2+\omega_{\mathrm{d}}^{\ 2}}-\dfrac{\zeta\omega_{\mathrm{n}}}{\omega_{\mathrm{d}}}\cdot\dfrac{\omega_{\mathrm{d}}}{(s+\zeta\omega_{\mathrm{n}})^2+\omega_{\mathrm{d}}^{\ 2}}]\end{array}\right\}\end{aligned} \tag{10}$$

where $f_{\mathrm{ref}}(s)=1/s$ is the per-unit signal, $\Delta f(s)=G_{\mathrm{PL\to f}}(s)/s$ denotes the frequency deviation, and ω_{d} stands for the damped frequency, which is expressed as:

$$\omega_{\mathrm{d}}=\omega_{\mathrm{n}}\sqrt{1-\xi^2} \tag{11}$$

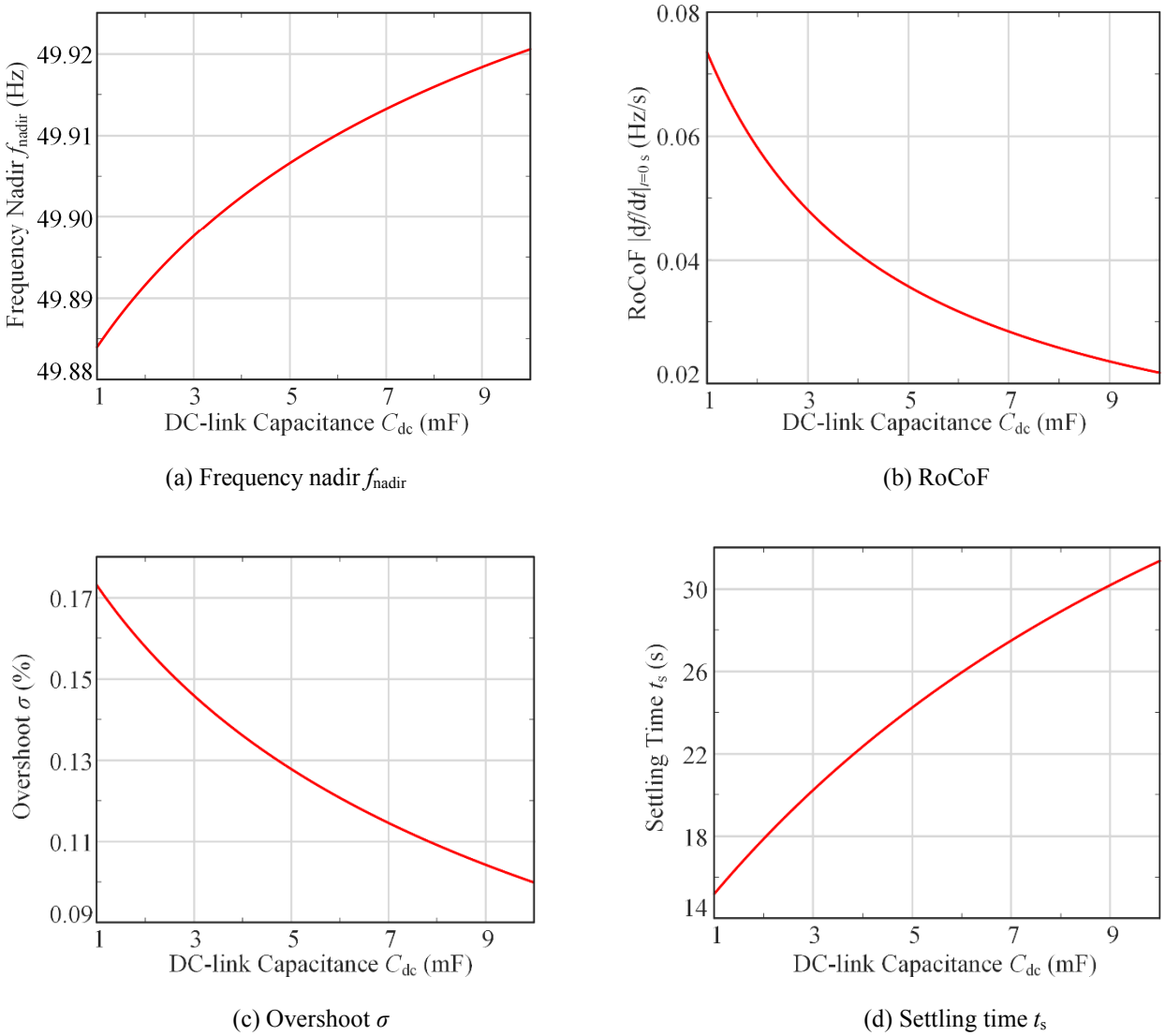

(a) Frequency nadir f_{nadir}

(b) RoCoF

(c) Overshoot σ

(d) Settling time t_s

Fig. 4. Relationship between dynamic indices and the DC-link capacitance C_{dc}.

By taking the inverse Laplace transform of (10), the expression of the grid frequency in the time domain can be derived as:

$$f(t) = 1 + G_0 \frac{z_1}{\omega_n^{\,2}} - G_0 e^{-\zeta\omega_n t} A_1 \sin(\omega_d t + \alpha) \tag{12}$$

where

$$\begin{cases} A_1 = \sqrt{\left(\dfrac{z_1}{\omega_n^{\,2}}\right)^2 + \left(\dfrac{-z_1\zeta + \omega_n}{\omega_n \omega_d}\right)^2} \\ \alpha = \arctan\left[\dfrac{\omega_d z_1}{(z_1\zeta - \omega_n)\omega_n}\right] \end{cases} \tag{13}$$

Based on (12), some important dynamic indices of the frequency regulation can be derived. The RoCoF is obtained by differentiating (12) with respect to time as:

$$\text{RoCoF} = \frac{d}{dt} f(t) = G_0 \begin{bmatrix} \zeta\omega_n e^{-\zeta\omega_n t} A_1 \sin(\omega_d t + \alpha) \\ -e^{-\zeta\omega_n t} A_1 \omega_d \cos(\omega_d t + \alpha) \end{bmatrix} \tag{14}$$

By setting (14) to zero, the time of the frequency nadir t_{nadir} can be derived as:

$$t_{nadir} = \frac{1}{\omega_d} \cdot \left[\arctan\left(\frac{\sqrt{1-\zeta^2}}{\zeta}\right) - \alpha + \pi \right] \tag{15}$$

Taking (15) into (12), the frequency nadir f_{nadir} can be obtained as:

$$f_{nadir} = 1 + \frac{G_0 z_1}{\omega_n^{\,2}} + G_0 e^{-\zeta\omega_n t_{nadir}} A_1 \sqrt{1-\zeta^2} \tag{16}$$

Then, based on (12) the steady-state frequency f_{ss} can be expressed as:

$$f_{ss}=1+\frac{G_0 z_1}{\omega_n^2} \tag{17}$$

Therefore, the frequency overshoot σ can be derived from (16) and (17) as:

$$\sigma=\left|\frac{f_{ss}-f_{nadir}}{f_{ss}}\right|\times 100\%=\left|\frac{e^{-\zeta\omega_n t_{nadir}}A_1\sqrt{1-\zeta^2}}{1+\frac{G_0 z_1}{\omega_n^2}}\right|\times 100\% \tag{18}$$

Additionally, the settling time (time for entering the 2% quasi-steady-state error band) can be derived as:

$$\begin{aligned}&\left|\frac{f_{ss}-f_{nadir}}{1-f_{ss}}\right|\times 100\%=2\%\Rightarrow\frac{\omega_n^2 e^{-\zeta\omega_n t_s}A_1}{z_1}=2\%\\&\Rightarrow t_s=-\frac{1}{\zeta\omega_n}\ln\left(\frac{0.02 z_1}{A_1\omega_n^2}\right)\end{aligned} \tag{19}$$

From the above analysis, the RoCoF, frequency nadir f_{nadir}, overshoot σ and the settling time t_s are functions of the DC-link capacitance C_{dc}. According to (14), (16), (18) and (19), the relationships between these dynamic indices and the DC-link capacitance are depicted in Fig. 4, and the parameters for obtaining Fig. 4 are listed in Table □.

TABLE I. SYSTEM PARAMETERS

Symbol	Description	Value
T_{RH}	Time constant of reheater	7.0 s
F_{HP}	Turbine HP coefficient	0.1 s
R	Droop coefficient	0.015
H	Inertia constant of SG	5.0 s
D	Damping coefficient	1.0
K_{fv}	Proportional gain	22.5
V_{dc_ref}	Rated DC-link voltage	400 V
ΔV_{dc_max}	Maximum DC-link voltage deviation	36 V
Δf_{max}	Maximum frequency deviation	0.2 Hz
VA_{rated}	Power rating	1000 kVA

From Fig. 4, it can be observed that when the DC-link capacitance increases, on one hand, the frequency nadir f_{nadir} rises, the RoCoF as well as the overshoot σ decrease, implying a better virtual inertia supportability from the GCCs. On another hand, the settling time t_s increases accordingly, indicating that it takes a longer time for the frequency to reach its quasi-steady state. Moreover, if the settling time t_s is too long, oscillation may be triggered, and instability issues will be resulted as claimed in [18]. Thus, the DC-link capacitance has critical impacts on the dynamic frequency response for GCCs providing virtual inertia, and as for the selection of the DC-link capacitance, there is a trade-off between the virtual inertia supportability and the settling time of the grid frequency.

B. Selection of the DC-Link Capacitance

As reported in [18, 19], the damping ratio ξ can be seen as a judgement to evaluate the dynamic performance for second order systems, and it has been verified in [20] that when ξ is within the range from 0.40 to 0.80, the satisfactory response of a control system can be guaranteed in most operating conditions. Thus, on the premise that the requirements of the frequency nadir and the RoCoF are satisfied, the DC-link capacitance can be selected through tuning the damping ratio ξ within its optimal range, i.e. 0.40 to 0.80, hence an appropriate dynamic performance can be ensured. According to (9), the relationship between the damping ratio ξ and the DC-link capacitance C_{dc} is depicted in Fig. 5. From Fig. 5, for the parameters given in Table □, when C_{dc} = 2.9 mF, ξ = 0.40, implying that the satisfactory dynamic response of the frequency regulation can be achieved if the DC-link capacitance C_{dc} is less than 2.9 mF.

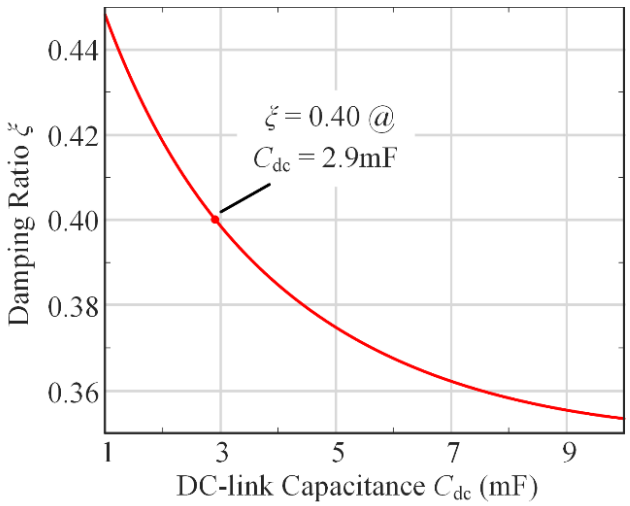

Fig. 5. Relationship between the damping ratio ξ and the DC-link capacitance C_{dc}.

IV. SIMULATION RESULTS

The impacts of the DC-link capacitance on the dynamic performance of GCCs supplying virtual inertia are successfully verified in simulations. The structure of the power system in simulations is shown in Fig. 6, where a three-phase SG supplies a GCC and the three-phase resistive loads. The simulation results of the frequency responses with different C_{dc} (1.0 mF, 2.7 mF and 9.0 mF) when subjected to a 4% step-up load change are shown in Fig. 7.

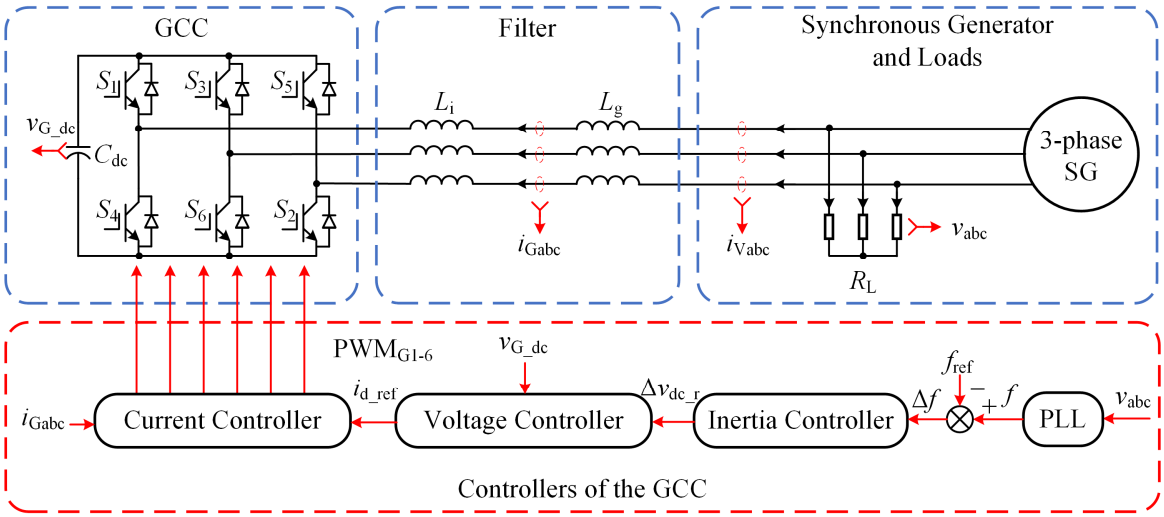

Fig. 6. Schematic of the simulation power system.

From Fig. 7, it can be observed that when C_{dc} increases, the frequency nadir rises, the RoCoF at t = 0 s declines, while the settling time of the grid frequency grows, which is consistent with the analysis in Section □. Moreover, when C_{dc} = 9.0 mF, which is far beyond the range derived in Section □, is applied to the GCC, the settling time is more than 30 s. When C_{dc} =2.7 mF, which is in the range derived in Section □, is applied to the GCC, the settling time is less than 20 s., an a balance between the virtual inertia supportability and the settling time is realized. Thus, the DC-link capacitance selection method presented in Section □ can help the system get a satisfactory dynamic response after disturbances.

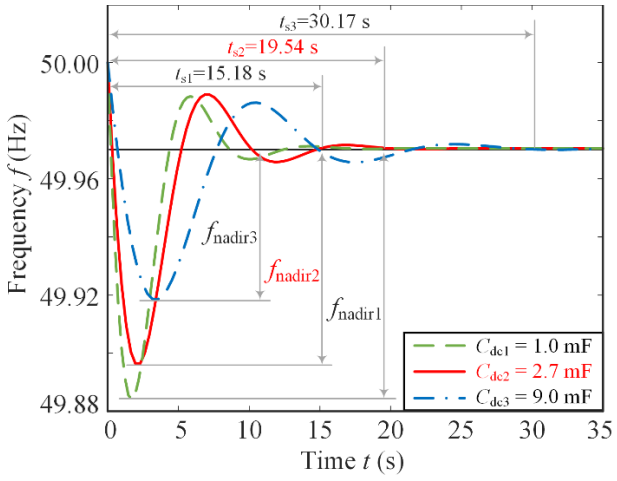

Fig. 7. Simulation results of the frequency response with different DC-link capacitance C_{dc}.

V. Conclusions

In the context of GCCs providing virtual inertia, the emulated inertia is in proportion with the DC-link capacitance, and thus the DC-link capacitance can affect the dynamic performance through modifying the virtual inertia constant. In this paper, the impacts of the DC-link capacitance on the dynamic performance of GCCs mimicking virtual inertia are studied, and the selection approach of the DC-link capacitance by tuning the damping ratio within its optimal range is presented. With the presented approach, the balance between the virtual inertia supportability and the frequency regulation settling time can be reached. The correctness is verified with simulations.

References

[1] J.-C. Feng, J. Yan, Z. Yu, X. Zeng, and W. Xu, "Case study of an industrial park toward zero carbon emission," Applied Energy, vol. 209, pp. 65-78, 2018.

[2] REN21, "Renewables 2017 Global Status Report," REN21 Secretaria, Paris2017.

[3] P. Kundur, N. J. Balu, and M. G. Lauby, Power system stability and control. McGraw-hill New York, 1994.

[4] F. Blaabjerg, R. Teodorescu, M. Liserre, and A. V. Timbus, "Overview of Control and Grid Synchronization for Distributed Power Generation Systems," IEEE Transactions on Industrial Electronics, vol. 53, no. 5, pp. 1398-1409, 2006.

[5] AEMO, "Black System South Australia 28 September 2016," 2017.

[6] H.-P. Beck and R. Hesse, "Virtual synchronous machine," in Electrical Power Quality and Utilisation, 2007. EPQU 2007. 9th International Conference on, 2007, pp. 1-6: IEEE.

[7] S. Wang, J. Hu, X. Yuan, and L. Sun, "On Inertial Dynamics of Virtual-Synchronous-Controlled DFIG-Based Wind Turbines," IEEE Transactions on Energy Conversion, vol. 30, no. 4, pp. 1691-1702, 2015.

[8] Y. Fu, Y. Wang, and X. Zhang, "Integrated wind turbine controller with virtual inertia and primary frequency responses for grid dynamic frequency support," IET Renewable Power Generation, vol. 11, no. 8, pp. 1129-1137, 2017.

[9] I. D. Margaris, S. A. Papathanassiou, N. D. Hatziargyriou, A. D. Hansen, and P. Sorensen, "Frequency Control in Autonomous Power Systems With High Wind Power Penetration," IEEE Transactions on Sustainable Energy, vol. 3, no. 2, pp. 189-199, 2012.

[10] A. Hosseinipour and H. Hojabri, "Virtual inertia control of PV systems for dynamic performance and damping enhancement of DC microgrids

with constant power loads," IET Renewable Power Generation, vol. 12, no. 4, pp. 430-438, 2018.

[11] K. Ping-Kwan, L. Pei, H. Banakar, and O. Boon Teck, "Kinetic Energy of Wind-Turbine Generators for System Frequency Support," IEEE Transactions on Power Systems, vol. 24, no. 1, pp. 279-287, 2009.

[12] J. Morren, S. W. H. de Haan, W. L. Kling, and J. A. Ferreira, "Wind Turbines Emulating Inertia and Supporting Primary Frequency Control," IEEE Transactions on Power Systems, vol. 21, no. 1, pp. 433-434, 2006.

[13] Y. Li, Z. Xu, and K. P. Wong, "Advanced control strategies of PMSG-based wind turbines for system inertia support," IEEE Transactions on Power Systems, vol. 32, no. 4, pp. 3027-3037, 2017.

[14] A. B. T. Attya and J. L. Dominguez-Garcia, "Insights on the provision of frequency support by wind power and the impact on energy systems," IEEE Transactions on Sustainable Energy, pp. 1-1, 2017.

[15] J. Fang, H. Li, Y. Tang, and F. Blaabjerg, "Distributed Power System Virtual Inertia Implemented by Grid-Connected Power Converters," IEEE Transactions on Power Electronics, 2017.

[16] J. Machowski, J. Bialek, J. R. Bumby, and J. Bumby, Power system dynamics and stability. John Wiley & Sons, 1997.

[17] P. M. Anderson and M. Mirheydar, "A Low-Order System Frequency Response Model," IEEE Transactions on Power Systems, vol. 5, no. 3, p. 10, 1990.

[18] F. Wang, L. Zhang, X. Feng, and H. Guo, "An Adaptive Control Strategy for Virtual Synchronous Generator," IEEE Transactions on Industry Applications, pp. 1-1, 2018.

[19] O. Jacobs, "The damping ratio of an optimal control system," IEEE Transactions on Automatic Control, vol. 10, no. 4, pp. 473-476, 1965.

[20] S. M. Shinners, Modern control system theory and design. John Wiley & Sons, 1998.